

Lawrence Berkeley National Laboratory

Recent Work

Title

Bedrock weathering contributes to subsurface reactive nitrogen and nitrous oxide emissions

Permalink

<https://escholarship.org/uc/item/28k495jd>

Journal

Nature Geoscience, 14(4)

ISSN

1752-0894

Authors

Wan, J
Tokunaga, TK
Brown, W
et al.

Publication Date

2021-04-01

DOI

10.1038/s41561-021-00717-0

Peer reviewed

**Bedrock weathering contributes to subsurface reactive nitrogen and nitrous
oxide emissions**

Jiamin Wan^{1*}, Tetsu K. Tokunaga^{1*}, Kenneth H. Williams¹, Wendy Brown², Alexander M.
Newman², Wenming Dong¹, Markus Bill¹, Curtis A. Beutler², Amanda N. Henderson², Nydra
Harvey-Costello¹, Mark E. Conrad¹, Nicholas J. Bouskill¹, Susan S. Hubbard¹

¹Earth and Environment Sciences Area, Lawrence Berkeley National Laboratory, Berkeley,
California, 94720

²Rocky Mountain Biological Laboratory, Crested Butte, Colorado, 81224

11 Atmospheric nitrous oxide contributes directly to global warming, yet models of the nitrogen
12 cycle do not account for bedrock, the largest pool of terrestrial nitrogen, as a source of nitrous
13 oxide. Although it is known that release rates of nitrogen from bedrock are large, there is an
14 incomplete understanding of the connection between bedrock-hosted nitrogen and atmospheric
15 nitrous oxide. Here, we quantify nitrogen fluxes and mass balances at a hillslope underlain by
16 marine shale. We found that at this site bedrock weathering contributes 78% of the subsurface
17 reactive nitrogen, while atmospheric sources (commonly regarded as the sole sources of reactive
18 nitrogen in pristine environments) account for only the remaining 22%. About 56% of the total
19 subsurface reactive nitrogen denitrifies, including 14% emitted as nitrous oxide. The remaining
20 reactive nitrogen discharges in porewaters to a floodplain where additional denitrification likely
21 occurs. We also found that the release of bedrock nitrogen occurs primarily within the zone of
22 the seasonally fluctuating water table and suggest that the accumulation of nitrate in the vadoes
23 zone, often attributed to fertilization and soil leaching, may also include contributions from
24 weathered nitrogen-rich bedrock. Our hillslope study suggests that under oxygenated and
25 moisture-rich conditions, weathering of deep, nitrogen-rich bedrock makes an important
26 contribution to the nitrogen cycle.

N₂O is produced during both microbial nitrification and denitrification in terrestrial and aquatic systems^{1,2}. Predictions of N₂O production rates have been based on estimated rates of reactive nitrogen (reactive-N) inputs including N-fertilizers, manure, fossil fuel combustion, and natural atmospheric sources²⁻⁶, without accounting for large quantities of weathering released rock-N⁷⁻¹¹. In pristine environments, atmospheric deposition and biological fixation in soils are still commonly regarded as the sole natural sources for reactive-N^{12,13}, despite mounting evidence for the importance of rock-N release to surface waters from weathering⁷⁻¹¹. Bedrock constitutes the largest terrestrial N reservoir on Earth, with fine-grained shale and mudstone containing the largest N inventory⁷. In these rocks, N is associated with organic matter, with post-burial diagenetic processes altering a fraction of the organic-N to ammonium (NH₄⁺), which can be incorporated into silicate minerals and sorbed on clays^{11,14,15}. Shales are recognized for their high capacity to release solutes including C, N, and metals through chemical weathering^{16,17}. Current understanding and models associated with rock weathering inputs to ecosystems rely on rates of tectonic uplift and land surface erosion¹⁸⁻²¹ over long geological time scales. Determining regional and local bedrock-N weathering influxes to ecosystems is technically challenging², as is determining subsurface weathering rates. Additionally, there is a paucity of information on N₂O originating from transformations of bedrock released N, although measured N₂O emissions from shale-derived soils indicate this pathway is important²².

Our study was conducted in the East River watershed²³ in the Upper Colorado River Basin (Fig. 1), along a lower montane hillslope (Fig. 1b-c) underlain with Mancos Shale²⁴. This Cretaceous shale is broadly distributed throughout the southwestern United States, and releases elevated concentrations of major ions, trace elements, and potential contaminants from chemical weathering^{16,17}. Thus, the shale weathering fluxes are dominant contributions to the East River's seasonally varying water chemistry²⁵⁻²⁸. Five boreholes (Fig 1c-g) were drilled along a transect to obtain pore water and gas samples at different depths spanning the soil-to-bedrock continuum. Time-dependent hydrologic properties^{27,28}, including groundwater flow and water table depth were also measured over three years. The annual total N input from atmospheric deposition measured at the Gothic CASTNET station²⁹ located 5 km from the hillslope is 2.68 ± 0.22 kg N ha⁻¹y⁻¹. Based on other work in the mountainous regions of Colorado³⁰, the biological N fixation (BNF) rate was assumed to be roughly equivalent to the deposition rate, and this value is about 10% lower than the estimated globally averaged terrestrial BNF rate of 3.0 kg N ha⁻¹y⁻¹ ³¹.

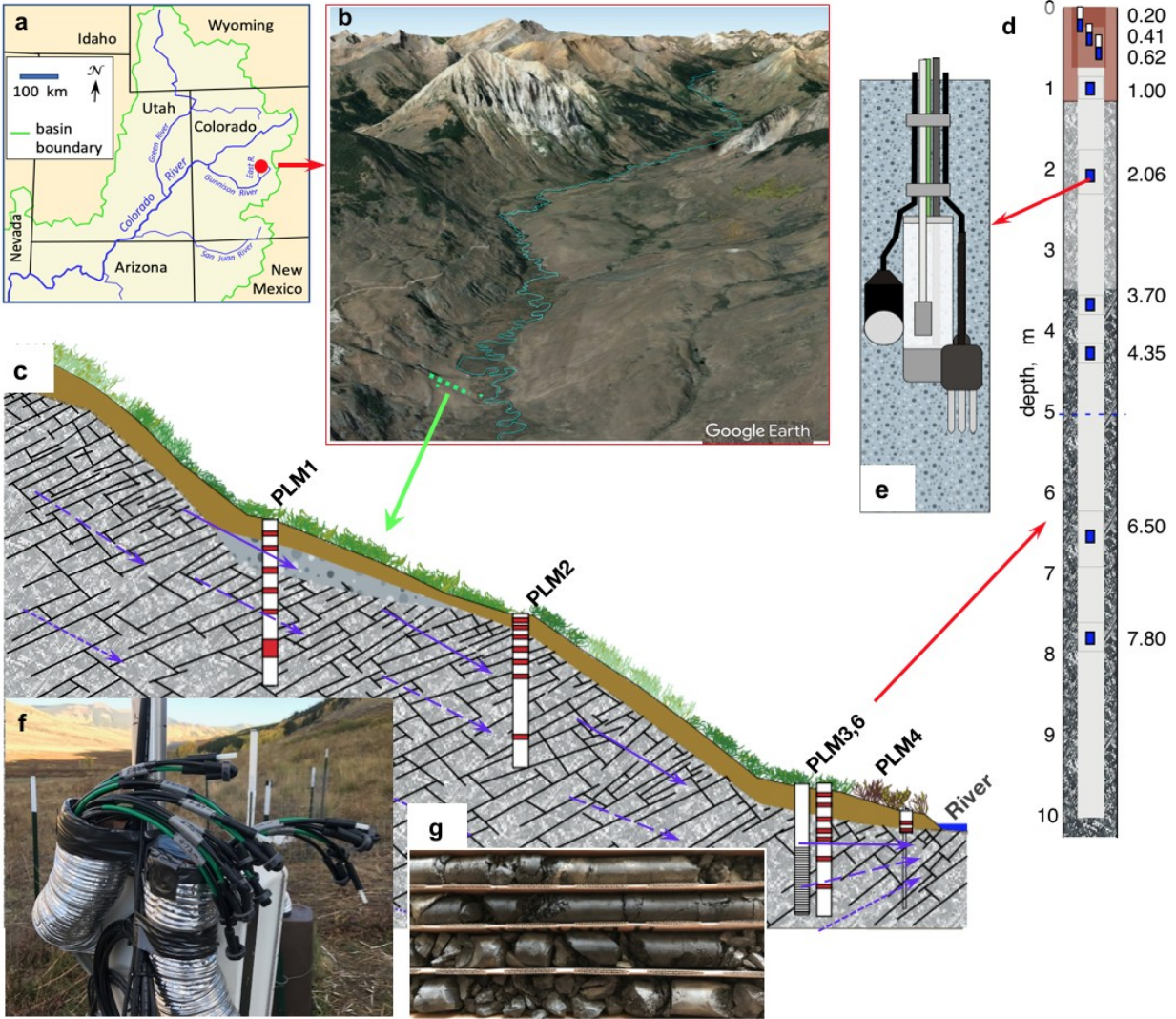


Fig. 1| The East River watershed study site and instrumentation. **a.** Colorado River Basin, with location of upper East River watershed indicated with the red dot. **b.** Google Earth view northward up the East River, showing location of the lower montane hillslope transect (green dotted line). **c.** Hillslope to floodplain transect showing five borehole locations. PLM3 and 6 are at the same elevation and 5 meters apart, located near the toe slope. PLM4 is located at the edge of the floodplain. Three boreholes PLM 1, 2, and 3 were instrumented for long term porewater and pore-gas sampling, and hydraulic measurements. **d.** Example of borehole cross-section showing instrumentation depths. **e.** Sensor/sampler units installed at selected depths consisted of a porewater sampler, moisture content sensor, thermistor, matric potential sensor, and gas sampler. **f.** Porewater and gas sampler access tubes. **g.** Rock cores (the soil samples were hand-augered).

Weathering is controlled by water table depth

Rock-N reentry into the labile reactive-N pool warrants a brief summary of the subsurface weathering mechanisms along the hillslope. The average soil thickness along the hillslope of 1.0 ± 0.3 m was determined using a hand-auger. We applied the established method of quantifying weathering depths through relative concentration $\tau_{i,j}$ ^{32,33} profiles of minerals (Methods). The profile average concentrations in the 4–10 m bgs interval were used to calculate the $\tau_{i,j}$ profiles (excluding a hot spot in PLM1). The unweathered bedrock contains on average 3.0% pyrite, 4.6% calcite, 7.5% dolomite, 7% plagioclase, and 30% illite. Pyrite, being ubiquitous in marine sedimentary rocks, is the most diagnostic mineral for weathering depth^{34,35}. Pyrite and carbonates are completely depleted ($\tau_j = -1$) down to about 2.0 m below ground surface (bgs), and the weathering fronts ($\tau_j = 0$) are at approximately 3.8, 4.2, and 3.3 m bgs at locations PLM1, 2, and 3, respectively (**Fig. 2a**). The measured annual water table depths at these locations over three years (**Fig. 2b**) show that the greatest depth to water table at each location matches the depth of the weathering front determined by the mineral relative concentration profiles (Fig. 2a), and that the vertical range of water table fluctuating defines the weathering zone (WZ). Products of shale pyrite and carbonate dissolution (SO_4^{2-} , H^+ , Ca^{2+} and Mg^{2+}) are clearly enriched in WZ pore waters relative to that in overlying soil and underlying fractured bedrock (**Fig. 2c**), consistent with the relative mineral concentration profiles. Optimal oxygen and moisture conditions for rapid chemical weathering occur in the fluctuating water table zone, hence delineated the WZ. Below the deepest water table elevation, oxygen diffusion is limited relative to the rapid microbial utilization of oxygen²⁷. Within the soil, the weathering reactive minerals, pyrite and carbonates, are depleted. Although hydrological controls on weathering have been recognized previously³⁶⁻³⁸, by coupling hydrological and geochemical field measurements we now can use seasonally fluctuating water table depths to predict subsurface weathering depths.

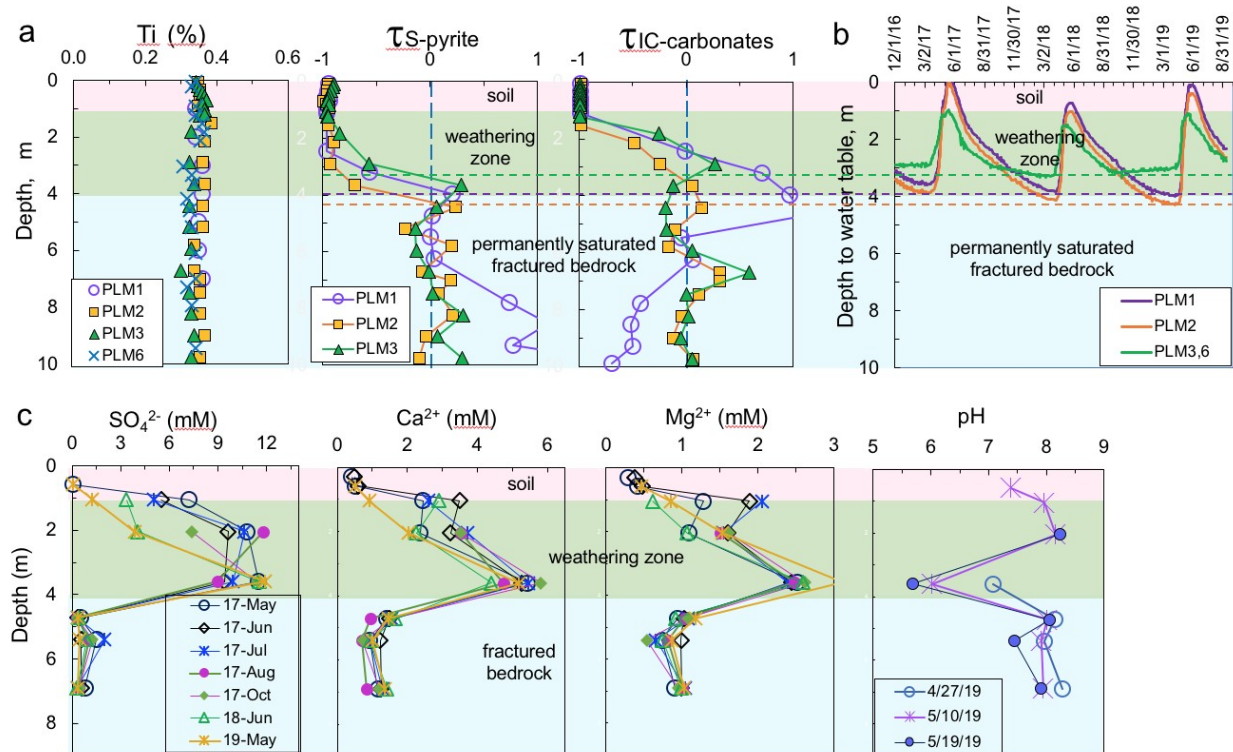


Fig. 2| Rock weathering occurs primarily below soil, within the depth zone of annually oscillating water table. a. Relative concentration-depth profiles of S-pyrite and IC-carbonate (uncertainties in τ are ≤ 0.09). Titanium (analytical uncertainty = 0.04%) served as the unremovable reference element in calculations. At $\tau_j = -1$, a mineral is completely depleted, and the depth crossing $\tau_j = 0$ (vertical dashed line) is used to identify weathering fronts. **b.** Time-dependent water table depths measured over the course of three years (depth uncertainties ≤ 0.05 m). The lowest water table depths (marked by horizontal dashed lines) match the depths of the weathering fronts determined by relative concentration-depth profiles (Fig. 2a). **c.** Depth profiles of dissolved species from the most weathering diagnostic minerals pyrite and carbonates and pH (note, the pH values were measured on spring 2019 only) in field pore waters from PLM1. Relative uncertainties in concentrations are ≤ 0.03 .

Subsurface reactive-N is mainly from rock weathering

Total nitrogen (TN) inventories in solid phase soil-bedrock at three locations along the hillslope are shown in **Fig. 3a**. The soil contains high TN, largely as organic-N in soil organic matter, and its concentrations rapidly decrease with depth, reaching the rock-N concentration at approximately 1.0 m bgs. The unweathered shale bedrock contains $0.13 \pm 0.032\%$ N, within the range found in slates, shales, and siltstones^{7,39}, equivalent to 32 Mg N ha^{-1} per 1.0 m thickness, a substantial source for N reentry into the terrestrial cycle through weathering. N-species concentration profiles released from a laboratory water leaching experiment (**Fig. 3b**) reflect immediately mobile N inventories, uninfluenced by field biogeochemical processes. These data provide several important insights: (1) In soil leachates the dominant N-species is dissolved organic-N (DON). (2) Rock leachates contain primarily NH_4^+ and DON, indicating the importance of inorganic-N (NH_4^+) released from clay minerals¹¹. (3) Extractable NO_3^- concentrations are negligible in soil and rock leachates. (4) The overall extractable total dissolved-N (TDN) concentrations in the shallower WZ (1.0 to 3.0 m bgs), are depressed, reflecting depletion of N within the WZ. **Fig. 3c** shows N-species concentration profiles in field porewaters collected over the course of 3 years. When compared with the laboratory leachates, these data reveal new understandings into subsurface weathering and N behavior. First, the TDN concentrations are several-fold higher in the WZ porewaters than in the overlying soil and underlying bedrock, indicating that the TDN is largely sourced from rock weathering. Secondly, NO_3^- is the dominant N-species within WZ porewaters, and is only present at high concentrations in the WZ, despite occurring at negligible concentrations in laboratory extracts of soil and rock, indicating significant nitrification of weathering-released NH_4^+ and DON. Mixing of soil and WZ porewaters occurs during snowmelt displacement of soil water into the WZ, and during water table rise of N-rich WZ porewaters into the soil. Low NO_3^- concentrations in the deepest WZ and bedrock porewaters are consistent with denitrification in these reducing zones. Pore-gas samples collected from soil and the WZ from May 2017 to May 2020 (**Fig. 3d**), show that nitrous oxide (N_2O) concentrations span three orders of magnitude, ranging from atmospheric concentrations (0.33 ppm) to over 200 ppm. These unique subsurface depth and time resolved N-species measurements provided part of the basis for calculating rates of N release and exports. The remaining necessary information requires quantifying rates of subsurface water flow and gas diffusion.

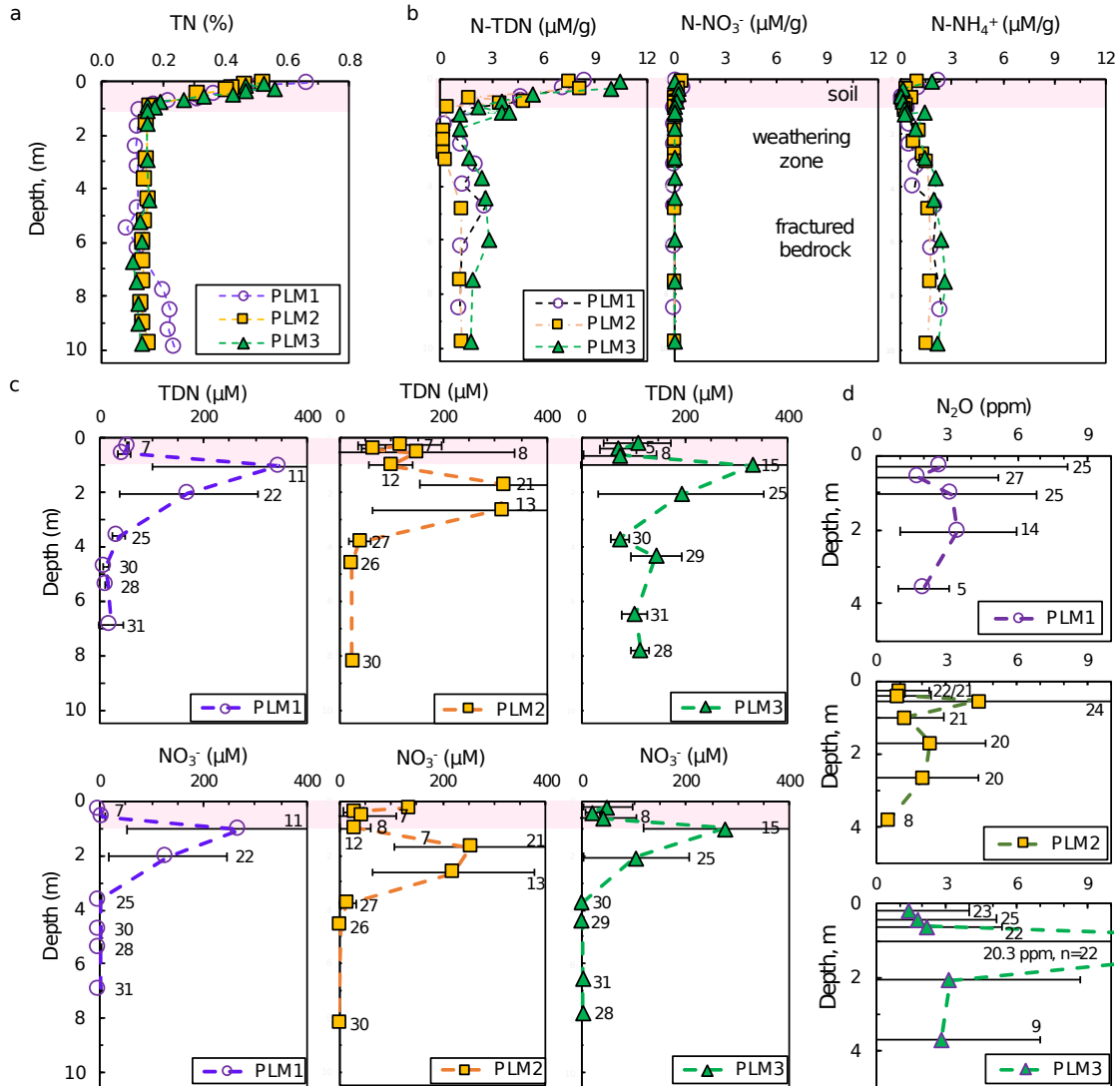


Fig. 3| The hillslope subsurface reactive-N is primarily from bedrock weathering, not from soil. **a.** Total nitrogen (TN) in soil-bedrock. The unweathered shale bedrock contains $0.13 \pm 0.032\%$ N (excluding a hot-spot). Relative uncertainties in individual values are ≤ 0.03 . **b.** N-species concentrations released from soil and rock through laboratory water leaching. Relative uncertainties in individual values are ≤ 0.03 . **c.** N-species concentration-depth profiles in field porewaters (averages of all samples, with the numbers of samples presented at each depth). Low matric potentials often prevented pore water collection in soil and WZ. NO₃⁻ appears in WZ porewaters only, showing that nitrification and mineralization transform the rock- and soil-released NH₄⁺ and DON to NO₃⁻. The fractured bedrock at PLM3, being located at the toe slope, receives some WZ pore waters from upslope regions. **d.** Depth-resolved N₂O concentrations in pore gas samples show elevated N₂O in nearly all the samples relative to the atmospheric concentration of approximately 0.33 ppm. Horizontal bars span ranges of measured values.

Rates of weathering, N-release, and N-exports

Time-dependent, fluxes of pore waters along the bedrock, WZ, and soil layers are needed to determine rates of hillslope bedrock weathering and dissolved-N export. Briefly, calculations of subsurface flow applied the transmissivity feedback method⁴⁰ to the three-layer (soil, WZ, fractured bedrock) system, with water mass balance constrained by annual precipitation minus evapotranspiration. In order to constrain predictions of subsurface flow and transport, these calculations were applied to two scenarios: one based on field-measured hydraulic conductivities, K , in each zone, and the other using amplified K values. Water mass conservation set the upper limit for amplified K in the soil and WZ to 25- and 1.5-times their measured values, respectively. The resulting calculated fluxes through the three subsurface zones and their dependence on water table depth are presented in **Fig. 4a1**. The results based on measured and enhanced K are represented by thin and thick curves, respectively.

Weathering was quantified as the annual export per unit watershed area of the sum of base cation equivalents ($BC = Na + 2Mg + K + 2Ca$)^{27,41}, using a correlation between specific conductance (SC) and BC (Methods, **Extended Data Fig. 1**). Measured SC trends (**Fig. 4a2**), show distinctions between the soil, WZ, and fractured bedrock zone, with the highest SC occurring within the WZ. By multiplying daily subsurface flow rates in each zone (**Fig. 4a1**) with their associated BC concentration (represented by SC in **Fig. 4a2**), daily BC export rates are obtained (**Fig. 4a3**). Because BC export rates are highest within the WZ, only exports from this zone and the total subsurface exports are shown in the green and blue trend lines, respectively. As before, the results based on measured and enhanced K are represented by thin and thick curves, respectively. Export rates increase during water table rise not only because the transmissive saturated zone becomes thicker, but also because flow mobilizes the solute-rich WZ pore waters. The BC export rate averaged from water year (WY) 2017 through WY2019 are 53.1 and 57.5 $\text{kmol}_e \text{ ha}^{-1} \text{ y}^{-1}$, for calculations based on the measured and enhanced K profiles, respectively. The average of these two scenarios and their differences are taken as the best estimate BC export rate and uncertainty, respectively, $55.3 \pm 4.4 \text{ kmol}_e \text{ ha}^{-1} \text{ y}^{-1}$.

Following similar rock mass balance analyses^{9,39}, the measured BC weathering rate of $55.3 \pm 4.4 \text{ kmol}_e \text{ ha}^{-1} \text{ y}^{-1}$ was scaled with the measured shale bedrock N:BC ratio = 0.0244 mol mol_e^{-1} , resulting in a rock-N release rate of $18.9 \pm 4.6 \text{ kg N ha}^{-1} \text{ y}^{-1}$. This rock-N release rate is greater than most literature values^{20,42}, indicating the importance of chemical weathering of N-rich sedimentary rocks. Comparing this rock-N influx with inputs from atmospheric deposition and estimated BNF (2.68 kg N ha^{-1} each), we find that 78% of the hillslope reactive-N originates from bedrock weathering. This quantification of N-influxes shows the overwhelming importance of reactive-N released through bedrock weathering at this hillslope underlain by weathering marine shale.

Advective transport of dissolved-N was calculated as the product of time-dependent Darcy fluxes and N concentrations within each zone. Temporal variations of NO_3^- and TDN concentrations in **Fig. 4a4 and 4a5** show their highest concentrations occurring in the WZ. Curves fit through average TDN values within each zone (**Fig. 4a5**) were multiplied by their respective Darcy fluxes (**Fig. 4a1**) to obtain the rates of TDN discharge in **Fig. 4a6** (Methods). Annual two-month periods with maximum snowmelt-driven transport are highlighted with blue backgrounds in **Fig. 4a1-6** to emphasize the strong seasonality of subsurface TDN export rates. These annual “hot moments” account for about 44% ($\pm 5\%$) of TDN exports. Per unit width of

the transect, average exports under the different *K* scenarios amount to 33 and 41 mol TDN m⁻¹ y⁻¹, equivalent to export rates of 9.5 and 11.8 kg of N ha⁻¹ y⁻¹, respectively. Thus, the representative TDN export rate is 10.6 ± 1.2 kg N ha⁻¹ y⁻¹ (**Extended Data Fig. 1**).

Rates of N loss by denitrification from the hillslope can be calculated from the difference between N-inputs (bedrock weathering and atmospheric sources including BNF) and N-outputs¹³. The denitrification rate calculated by subtracting pore water TDN exports from the sum of inputs is 13.6 ± 0.8 kg N ha⁻¹ y⁻¹, slightly greater than the sum of estimated global average watershed soil and groundwater denitrification rates, 12.04 kg N ha⁻¹ y⁻¹⁴³. Hillslope denitrification losses amount to 56% of the hillslope reactive-N inputs, 10% higher than the calculated global soil average of 46%⁴³. These denitrification rates obtained by subtracting outputs from inputs in order to close the hillslope N mass balance warrant comparisons with independent diffusion calculations. While N₂ is expected to be the dominant product of denitrification, its high atmospheric concentrations make the efflux from the subsurface difficult to quantify. In contrast, the low natural abundance of N₂O in the atmosphere facilitates calculations of its diffusive export (Methods). **Figure 4b1** shows time trends in N₂O concentrations collected from the shallow soil depths at the three hillslope locations, that permit calculation of diffusion gradients driving N₂O to the atmosphere (**Fig. 4b2**). The seasonal variations in shallow soil temperature (**Fig. 4b3**) and volumetric water content (**Fig. 4b4**) give rise to variations in the effective diffusion coefficient *D_e* for N₂O within the surface soils (**Fig. 4b5**). Time trends for N₂O effluxes to the atmosphere (**Fig. 4b6**) were obtained from the product of *D_e* and concentration gradients⁴⁴. The highest N₂O effluxes at all three locations occurred in winter of 2017–2018, a perplexing “hot moment”². The calculated N₂O flux rates (2017–2020) from the three locations amount to 5.9 ± 3.2 and 0.99 ± 0.75 kg N ha⁻¹ y⁻¹, with and without the “hot moment”, respectively, constitute 44% and 7% of the hillslope denitrification. The average and range of these values, 25 ± 18%, fall within the very wide range (77% to 1%; average of 20.7%) reported in a synthesis of studies of natural ecosystems. The overall hillslope N fluxes and mass balance are presented in **Extended Data Fig. 3**.

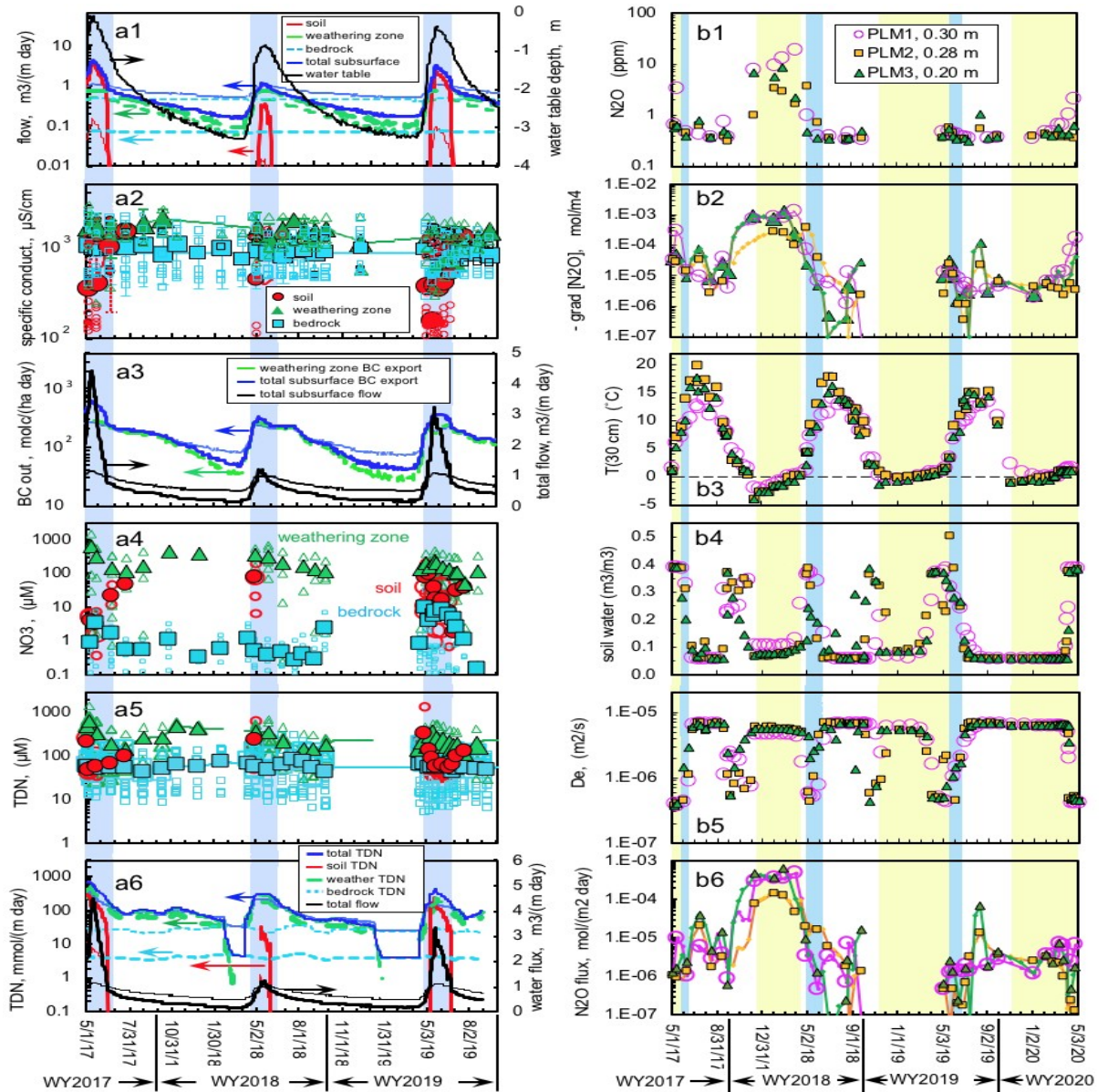
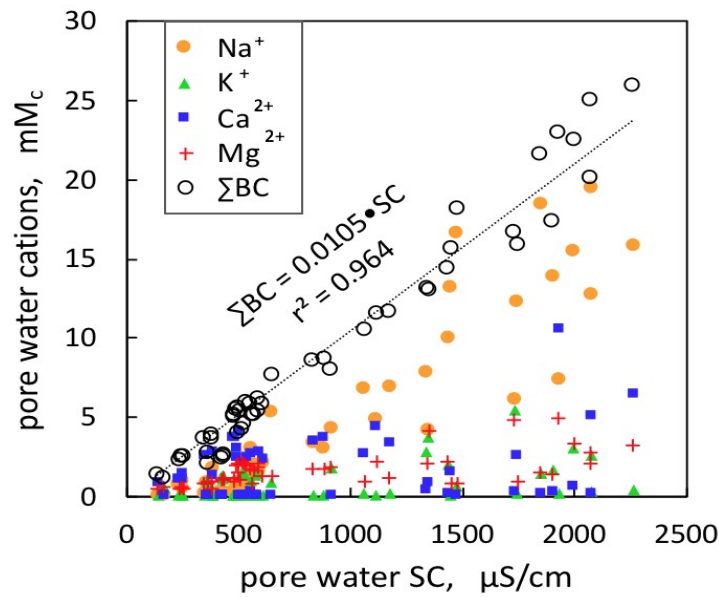


Fig. 4| Measurements and rates calculations of bedrock weathering (a1-3), dissolved-N export to hydrosphere (a4-6), and N₂O to atmosphere (b1-6). a1. Time- and depth-dependent downslope water fluxes in three zones using measured and amplified hydraulic conductivity (K). Here and elsewhere, results based on measured and enhance K are indicated by light and heavy curves, respectively, and constrain uncertainties in flow and transport rates. Arrows on curves point to associated axes. **a2.** Time- and depth-dependent specific conductance (SC) in the three zone porewaters. Larger symbols represent averages and vertical bars are standard errors. **a3.** Time- and depth-resolved total subsurface flow rates, and rates of base cation (BC) discharge for the WZ and total subsurface. **a4.** Temporal variation of NO₃⁻ and **a5.** Temporal variation of TDN within the three strata (relative standard deviations ≤ 0.03). The trend lines are fit through the average values. **a6.** TDN discharge fluxes within each subsurface zone obtained by multiplying pore water TDN trends by their respective Darcy fluxes. The light-blue shaded segments denote 2-month intervals with maximum subsurface flow and TDN discharge rates during each year. **b1.**

Time trends of soil gas N₂O concentrations within the surface soil (relative uncertainties ≤ 0.05). **b2.** N₂O concentration gradient, **b3.** soil temperature (uncertainties ≤ 1 °C), **b4.** volumetric water content (uncertainties ≤ 0.03), **b5.** effective N₂O diffusion coefficient (relative uncertainties ≤ 0.15), and **b6.** diffusive N₂O efflux to the atmosphere (relative uncertainties ≤ 0.2). The blue and yellow backgrounds indicate periods with highest water table positions and with snow cover, respectively.



Extended Data Fig. 1 | Correlations between the sum of separately measured base cations (ΣBC) and the specific conductance (SC) in porewaters. The measured SC values were used for weathering rates calculations.

	zone	K $m\ s^{-1}$	% of yearly N exported during maximum 2 months	TDN export rates		
				per unit transect width $\frac{mol}{m^{-1}\ y^{-1}}$	TDN per transect area $\frac{mol}{ha^{-1}\ y^{-1}}$ $kg\ ha^{-1}\ y^{-1}$	
measured K	surf. soil	9.70×10^{-6}	39%	0.22	4.5	0.06
	subsoil	7.90×10^{-6}		22.7	471	6.60
	WZ	1.10×10^{-5}		9.8	203	2.84
	FBR	1.60×10^{-7}		32.7	678	9.49
	total subsurface exports					
	% of yearly N exported during maximum 2 months					
enhanced K for soil and WZ	soil	2.42×10^{-4}	49%	5.4	113	1.6
	subsoil	1.98×10^{-4}		34.2	710	9.9
	WZ	1.65×10^{-5}		1.5	31	0.4
	FBR	1.60×10^{-7}		40.7	845	11.8
	total subsurface exports					
	% of yearly N exported during maximum 2 months					

Extended Data Fig. 2 | Summary of calculated subsurface total dissolved nitrogen (TDN export rates). The TDN concentrations and export rates are averaged from May 2017 to September 2019. Predictions using flow rates based on field-measured K and enhanced K (25x for soil, 1.5x for the WZ) are compared. In the table, WZ and FBR refer to the weathering zone and fractured bedrock, respectively. The importance of TDN export during the peak 2-month periods of snowmelt recharge is noteworthy, amounting to 39% and 49% of total exports, based on the measured and enhance K , respectively.

	measured <i>K</i>	enhanced <i>K</i>	average transport	measured <i>K</i>	enhanced <i>K</i>	average transport
	Import/Export rate Kg N ha ⁻¹ y ⁻¹			fraction of import or export		
atmospheric dep.	2.7	2.7	2.7	0.114	0.108	0.11
biological N-fix.	2.7	2.7	2.7	0.114	0.108	0.11
rock weathering N	18.1	19.6	18.9	0.77	0.78	0.78
porewater export	-9.5	-11.8	-10.6	-0.39	-0.49	-0.44
N ₂ + N ₂ O flux	-14.0	-13.2	-13.6	-0.58	-0.54	-0.56
N ₂ O flux			-3.5			-0.14

Extended Data Fig. 3 | Hillslope N mass balance. Nitrogen fluxes along the lower montane hillslope. The two different hydraulic conductivity (*K*) scenarios constrain N influxes from weathering and effluxes in groundwater flow and overall diffusion (N₂ + N₂O) to the atmosphere. The N₂O flux is the three-year average of diffusion calculations with and without inclusion of winter 2018-2019, for three locations.

Rock-N weathering release and implications

By integrating subsurface hydrological and biogeochemical measurements, quantitative understanding of the hillslope N cycle became possible (**Fig. 5**). Bedrock weathering occurs primarily within the zone of annual water table oscillation we defined as the WZ. At this site, about 78% of the total subsurface reactive-N is sourced from the WZ, contrary to the common belief that atmospheric sources are the sole N sources in pristine environments. High concentrations of nitrate accumulate in WZ porewaters, mostly from nitrification of bedrock-derived NH₄⁺ and DON. Thus, the widely observed NO₃⁻ accumulation in the vadose zone generally attributed to fertilization and soil leaching⁴⁵ can also reflect subsurface weathering in regions where N-containing bedrock is under favorable oxidizing and moisture conditions¹¹.

The importance of bedrock-N contributions to global N₂O emissions becomes evident upon inspection of global N-fluxes. About 10–18 Tg rock-N y⁻¹ is released globally^{9,31}. Applying our measured 56% denitrification of reactive-N with 25% of denitrification lost as N₂O, extrapolates to 1.4 to 2.5 Tg N-N₂O y⁻¹ sourced from bedrock weathering globally. A similar range of 1.0 to 1.7 Tg N-N₂O y⁻¹ is obtained solely from literature review values of terrestrial N fluxes, using 46% denitrification⁴³ and 21% of denitrified N lost as N₂O. The latter value was taken from a review that summarized results from 9 natural field sites. Our determination that 25% of denitrified N is lost as N₂O is well within 1 standard error of the average (20.7% ± 7.9%) reported in this review. Thus, our study is consistent with others' results, and provides a framework for investigations into the fate of rock-N in other settings. The underlying assumptions are that the rock-N releases can be quantified through combining measured rock weathering profiles with export calculations of dissolved N and gaseous N₂O. Uncertainties associated with the aqueous fluxes were constrained with upper and lower estimates of pore water velocities, while the gaseous flux uncertainty was constrained by including and excluding an apparent N₂O hot moment efflux. Both our study and calculations based solely on literature values suggest that the global terrestrial N-N₂O flux (10.0 ± 2.0 Tg N-N₂O y⁻¹)⁵ includes a

significant and previously unrecognized contribution of roughly 10 to 20% from bedrock weathering.

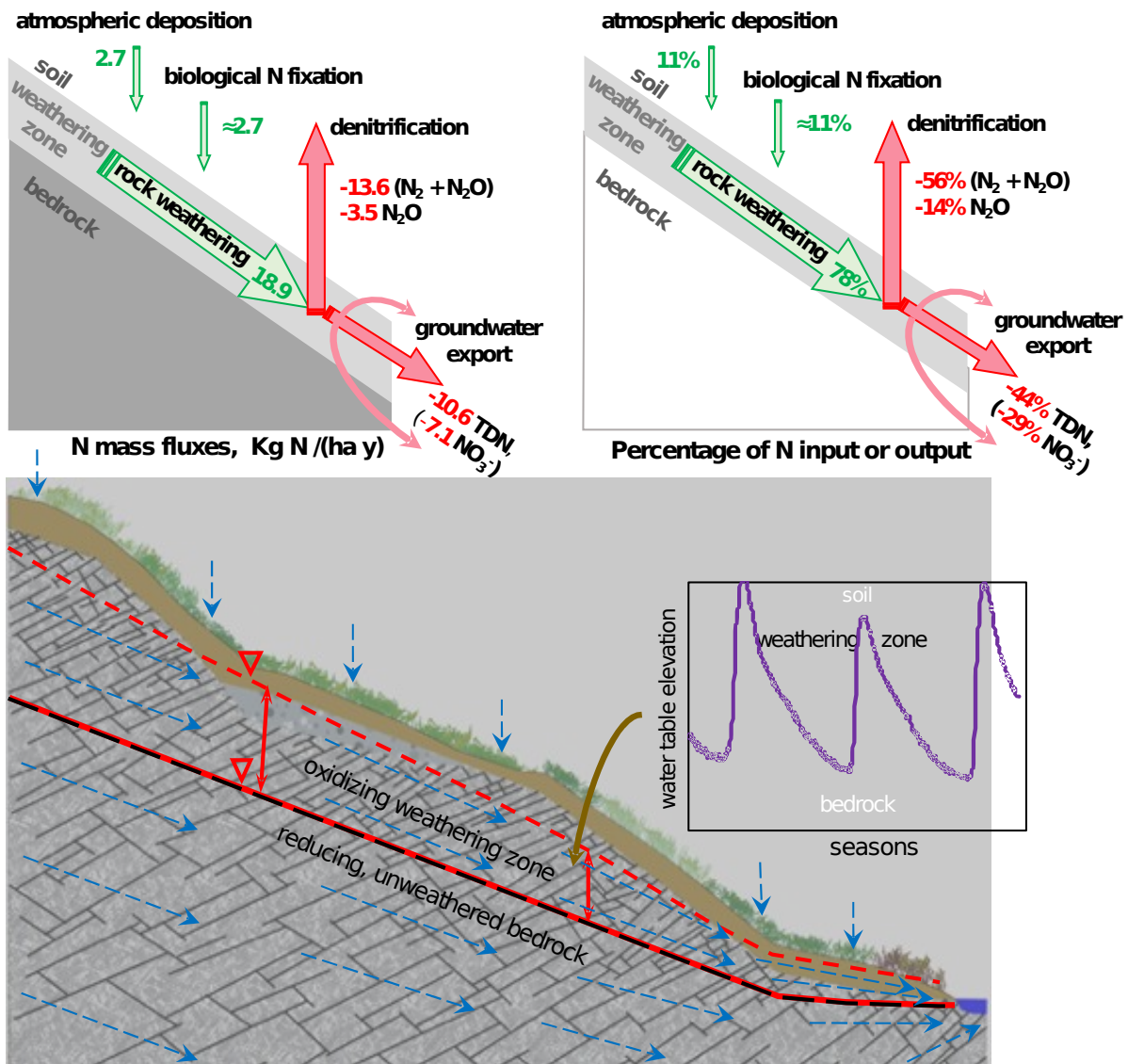


Fig. 5 | Conceptual model for hillslope bedrock-N weathering release and exports with N mass balance. The hillslope N mass fluxes (a, b) indicate that the influx rates from bedrock-N release are over three times greater than that of the combined atmospheric deposition and BNF. About $77 \pm 14\%$ of the TDN export from the hillslope subsurface to floodplain occurs along the WZ, with $44 \pm 5\%$ of it occurring during the two-month period of maximum snowmelt-driven flow. Denitrification losses about 56% of the total subsurface reactive N, with more than a quarter of it attributable to N₂O. Weathering is controlled by water table depth, within the fluctuating water table zone (c, d), where the optimal oxygen and moisture conditions promote rapid biogeochemical reactions.

319 References

- 320 1 Bremner, J. M. Sources of nitrous oxide in soils. *Nutr Cycl Agroecosys* **49**, 7-16 (1997).
- 321 2 Bouwman, A. F. *et al.* Global trends and uncertainties in terrestrial denitrification and
- 322 N₂O emissions. *Philos T R Soc B* **368**, doi:10.1098/rstb.2013.0112 (2013).
- 323 3 Ravishankara, A. R., Daniel, J. S. & Portmann, R. W. Nitrous Oxide (N₂O): The
- 324 Dominant Ozone-Depleting Substance Emitted in the 21st Century. *Science* **326**, 123-125
- 325 (2009).
- 326 4 Thompson, R. L. *et al.* Acceleration of global N₂O emissions seen from two decades of
- 327 atmospheric inversion. *Nature Climate Change* **9**, 993 (2019).
- 328 5 Tian, H. Q. *et al.* Global soil nitrous oxide emissions since the preindustrial era estimated
- 329 by an ensemble of terrestrial biosphere models: Magnitude, attribution, and uncertainty.
- 330 *Global Change Biology* **25**, 640-659 (2019).
- 331 6 Butterbach-Bahl, K., Baggs, E. M., Dannenmann, M., Kiese, R. & Zechmeister-
- 332 Boltenstern, S. Nitrous oxide emissions from soils: how well do we understand the
- 333 processes and their controls? *Philos T R Soc B* **368**, 1621 (2013).
- 334 7 Johnson, B. & Goldblatt, C. The nitrogen budget of Earth. *Earth-Sci Rev* **148**, 150-173
- 335 (2015).
- 336 8 Holloway, J. M. & Dahlgren, R. A. Nitrogen in rock: Occurrences and biogeochemical
- 337 implications. *Global Biogeochem. Cycles* **16**, doi:10.1029/2002gb001862 (2002).
- 338 9 Houlton, B. Z., Morford, S. L. & Dahlgren, R. A. Convergent evidence for widespread
- 339 rock nitrogen sources in Earth's surface environment. *Science* **360**, 58-62 (2018).
- 340 10 Morford, S. L., Houlton, B. Z. & Dahlgren, R. A. Direct quantification of long-term rock
- 341 nitrogen inputs to temperate forest ecosystems. *Ecology* **97**, 54-64 (2016).
- 342 11 Sullivan, P. J., Sposito, G., Strathouse, S. M. & Hansen, C. L. Geologic nitrogen and the
- 343 occurrence of high nitrate soils in the western San-Joaquin Valley, California. *Hilgardia*
- 344 **47**, 15-49 (1979).
- 345 12 Butterbach-Bahl, K. *et al.* in *The European Nitrogen Assessment* (eds M. A. Sutton *et*
- 346 *al.*) Ch. 6, 664, Cambridge University Press (2011).
- 347 13 Van Breemen, N. *et al.* Where did all the nitrogen go? Fate of nitrogen inputs to large
- 348 watersheds in the northeastern USA. *Biogeochemistry* **57**, 267-293 (2002).
- 349 14 Williams, L. B., Wilcoxon, B. R., Ferrell, R. E. & Sassen, R. Diagenesis of Ammonium
- 350 during Hydrocarbon Maturation and Migration, Wilcox-Group, Louisiana, USA. *Appl.*
- 351 *Geochem.* **7**, 123-134 (1992).
- 352 15 Muller, P. J. C/N ratios in Pacific deep-sea sediments: Effect of inorganic ammonium and
- 353 organic nitrogen compounds sorbed by clays. *Geochimica et Cosmochimica Acta.* **41**,
- 354 765-776 (1977).
- 355 16 Morrison, S. J., Goodknight, C. S., Tigar, A. D., Bush, R. P. & Gil, A. Naturally
- 356 Occurring Contamination in the Mancos Shale. *Environmental Science & Technology* **46**,
- 357 1379-1387 (2012).
- 358 17 Tuttle, M. L. W., Fahy, J. W., Elliott, J. G., Grauch, R. I. & Stillings, L. L. Contaminants
- 359 from Cretaceous black shale: II. Effect of geology, weathering, climate, and land use on
- 360 salinity and selenium cycling, Mancos Shale landscapes, southwestern United States.
- 361 *Appl. Geochem.* **46**, 72-84 (2014).

362 18 Riebe, C. S., Kirchner, J. W. & Finkel, R. C. Long-term rates of chemical weathering and
363 physical erosion from cosmogenic nuclides and geochemical mass balance. *Geochim.*
364 *Cosmochim. Acta* **67**, 4411-4427 (2003).

365 19 Montgomery, D. R. & Brandon, M. T. Topographic controls on erosion rates in
366 tectonically active mountain ranges. *Earth. Planet. Sci. Lett.* **201**, 481-489 (2002).

367 20 Morford, S. L., Houlton, B. Z. & Dahlgren, R. A. Geochemical and tectonic uplift
368 controls on rock nitrogen inputs across terrestrial ecosystems. *Global Biogeochem.*
369 *Cycles* **30**, 333-349 (2016).

370 21 West, A. J., Galy, A. & Bickle, M. Tectonic and climatic controls on silicate weathering.
371 *Earth. Planet. Sci. Lett.* **235**, 211-228 (2005).

372 22 Holloway, J. M. & Smith, R. L. Nitrogen and carbon flow from rock to water: Regulation
373 through soil biogeochemical processes, Mokelumne River watershed, California, and
374 Grand Valley, Colorado. *J Geophys Res-Earth* **110**, doi:Artn F01010
375 10.1029/2004jf000124 (2005).

376 23 Hubbard, S. S. *et al.* The East River, Colorado, Watershed: A mountainous community
377 testbed for improving predictive understanding of multiscale hydrological-
378 biogeochemical dynamics. *Vadose Zone Journal* **17**, doi:ARTN 180061
379 10.2136/vzj2018.03.0061 (2018).

380 24 Gaskill, D. L., Mutschler, F. E., Kramer, J. H., Thomas, J. A. & Zahoney, S. G. Geologic
381 map of the Gothic Quadrangle, Colorado, Gunnison County, Department of Interior, U.S.
382 Geological Survey (1991).

383 25 Carroll, R. W. H. *et al.* Factors controlling seasonal groundwater and solute flux from
384 snow-dominated basins. *Hydrological Processes* **32**, 2187-2202 (2017).

385 26 Winnick, M. J. *et al.* Snowmelt controls on concentration-discharge relationships and the
386 balance of oxidative and acid-base weathering fluxes in an alpine catchment, East River,
387 Colorado. *Water Resour. Res.* **53**, 2507-2523 (2017).

388 27 Wan, J. M. *et al.* Predicting sedimentary bedrock subsurface weathering fronts and
389 weathering rates. *Sci Rep-Uk* **9**, doi:10.1038/s41598-019-53205-2 (2019).

390 28 Tokunaga, T. K. *et al.* Depth- and Time-Resolved Distributions of Snowmelt-Driven
391 Hillslope Subsurface Flow and Transport and Their Contributions to Surface Waters.
392 *Water Resour Res* **55**, 9474-9499 (2019).

393 29 CASTNET (United States Environmental Protection Agency) (2019).

394 30 Darrouzet-Nardi, A., Erbland, J., Bowman, W. D., Savarino, J. & Williams, M. W.
395 Landscape-level nitrogen import and export in an ecosystem with complex terrain,
396 Colorado Front Range. *Biogeochemistry* **109**, 271-285 (2012).

397 31 Vitousek, P. M., Menge, D. N. L., Reed, S. C. & Cleveland, C. C. Biological nitrogen
398 fixation: rates, patterns and ecological controls in terrestrial ecosystems. *Philos T R Soc B*
399 **368**, doi:10.1098/rstb.2013.0119 (2013).

400 32 Anderson, S. P., Dietrich, W. E. & Brimhall, G. H. Weathering profiles, mass-balance
401 analysis, and rates of solute loss: Linkages between weathering and erosion in a small,
402 steep catchment. *Geol Soc Am Bull* **114**, 1143-1158 (2002).

403 33 Brimhall, G. H. & Dietrich, W. E. Constitutive Mass Balance Relations between
404 Chemical-Composition, Volume, Density, Porosity, and Strain in Metasomatic

405 Hydrochemical Systems - Results on Weathering and Pedogenesis. *Geochim.*
406 *Cosmochim. Acta* **51**, 567-587 (1987).

407 34 Littke, R., Klusmann, U., Krooss, B. & Leythaeuser, D. Quantification of Loss of
408 Calcite, Pyrite, and Organic-Matter Due to Weathering of Toarcian Black Shales and
409 Effects on Kerogen and Bitumen Characteristics. *Geochim. Cosmochim. Acta* **55**, 3369-
410 3378 (1991).

411 35 Galy, A. & France-Lanord, C. Weathering processes in the Ganges-Brahmaputra basin
412 and the riverine alkalinity budget. *Chem. Geol.* **159**, 31-60 (1999).

413 36 Brantley, S. L. *et al.* Toward a conceptual model relating chemical reaction fronts to
414 water flow paths in hills. *Geomorphology* **277**, 100-117 (2017).

415 37 Manning, A. H., Verplanck, P. L., Caine, J. S. & Todd, A. S. Links between climate
416 change, water-table depth, and water chemistry in a mineralized mountain watershed.
417 *Appl. Geochem.* **37**, 64-78 (2013).

418 38 Torres, M. A., West, A. J. & Clark, K. E. Geomorphic regime modulates hydrologic
419 control of chemical weathering in the Andes-Amazon. *Geochim. Cosmochim. Acta* **166**,
420 105-128 (2015).

421 39 Holloway, J. M. & Dahlgren, R. A. Geologic nitrogen in terrestrial biogeochemical
422 cycling. *Geology* **27**, 567-570 (1999).

423 40 Rodhe, A. On the generation of stream runoff in till soils. *Nord Hydrol* **20**, 1-8 (1989).

424 41 Horton, T. W., Chamberlain, C. P., Fantle, M. & Blum, J. D. Chemical weathering and
425 lithologic controls of water chemistry in a high-elevation river system: Clark's Fork of the
426 Yellowstone River, Wyoming and Montana. *Water Resour. Res.* **35**, 1643-1655 (1999).

427 42 Holloway, J. M., Dahlgren, R. A., Hansen, B. & Casey, W. H. Contribution of bedrock
428 nitrogen to high nitrate concentrations in stream water. *Nature* **395**, 785-788 (1998).

429 43 Seitzinger, S. *et al.* Denitrification across landscapes and waterscapes: A synthesis.
430 *Ecological Applications* **16**, 2064-2090 (2006).

431 44 Tokunaga, T. K. *et al.* Deep Vadose Zone Respiration Contributions to Carbon Dioxide
432 Fluxes from a Semiarid Floodplain. *Vadose Zone J* **15**, doi:10.2136/vzj2016.02.0014
433 (2016).

434 45 Ascott, M. J. *et al.* Global patterns of nitrate storage in the vadose zone. *Nat Commun* **8**,
435 doi:ARTN 1416 10.1038/s41467-017-01321-w (2017).

436 46 Kendall, K. A., Shanley, J. B. & McDonnell, J. J. A hydrometric and geochemical
437 approach to test the transmissivity feedback hypothesis during snowmelt. *Journal of*
438 *Hydrology* **219**, 188-205 (1999).

439 47 Brooks, E. S., Boll, J. & McDaniel, P. A. A hillslope-scale experiment to measure lateral
440 saturated hydraulic conductivity. *Water Resour Res* **40**, doi:Artn W04208
441 10.1029/2003wr002858 (2004).

442 48 Moldrup, P. *et al.* Predicting the gas diffusion coefficient in repacked soil: Water-induced
443 linear reduction model. *Soil Science Society of America Journal* **64**, 1588-1594 (2000).

444 49 Massman, W. J. A review of the molecular diffusivities of H₂O, CO₂, CH₄, CO, O₃,
445 SO₂, NH₃, N₂O, NO, AND NO₂ in air, O₂ AND N₂ near STP. *Atmos. Environ.* **32**,
446 1111-1127 (1998).

447 50 Bowling, D. R. & Massman, W. J. Persistent wind-induced enhancement of diffusive CO₂
448 transport in a mountain forest snowpack. *J Geophys Res-Bioge* **116**, doi:Artn G04006
449 10.1029/2011jg001722 (2011).
450
451

Correspondence and requests for materials should be addressed to
Jiamin Wan, jwan@lbl.gov; and Tetsu K. Tokunaga, tktokunaga@lbl.gov

Acknowledgments

We thank the Rocky Mountain Biological Laboratory (RMBL) for helping with field research. This work was conducted as part of the Watershed Function Scientific Focus Area at Lawrence Berkeley National Laboratory and was supported by the U.S. Department of Energy (DOE) Subsurface Biogeochemical Research Program, DOE Office of Science, Office of Biological and Environmental Research, under Contract Number DE-AC02-05CH11231. Mention of trade names and commercial analytical services do not imply endorsement.

Author contributions

J.W., T.K.T. designed the research, conducted the data analyses, and wrote the manuscript; K.H.W. led the field team; T.K.T., K.H.W., A.M.N., W.B., C.A.B, A.N.H. performed field instrumentation, monitoring and sampling; J.W., W.D., M.B., N.H.-C, M.E.C., N.J.B. conducted laboratory measurements. S.S.H. contributed to the conceptual model and reviewed the manuscript.

Competing interests

The authors declare no competing interests.

Data availability

Data used in this paper are published on ESS-DIVE (<https://data.ess-dive.lbl.gov/>), which is freely accessible to the public with a data DOI for citation. ESS-DIVE is part of the DataONE network and is registered with fairsharing.org.

Methods

Study site. The study site²³ is situated in the Upper East River basin, a headwater mountainous watershed situated in the Upper Colorado River Basin (**Fig. 1a**). The watershed has an average elevation of 3266 m, with 1420 m of topographic relief. The area has a continental, subarctic climate with long and cold winters, short and cool summers, a mean annual temperature of 3°C and mean annual precipitation of about 680 mm (approximately 70% as snow). Excursions in river discharge are driven primarily by snowmelt in spring to early summer. This study was conducted along a northeast facing hillslope transect (**Fig. 1b**) that adjoins a riparian floodplain along the East River, which in turn drains into the Gunnison River, a major tributary of the Colorado River. The hillslope is vegetated with grasses, forbs, and shrubs representative of the regional lower montane meadow environments, and the majority of roots are shallower than 20 cm and seldom deeper than 1.0 m. The hillslope is underlain by Mancos Shale.

Field drilling, instrumentation, and hydraulic measurements. Along the hillslope to floodplain flow transect (**Fig. 1c**) we drilled five 10 m deep boreholes (0.14 m diameter) into the bedrock along a 137 m long hillslope transect, including one borehole in the floodplain. We collected the solid samples over the soil-to-bedrock continuum, and installed instruments (moisture sensors, pore water samplers, gas samplers) at different depths inside the boreholes for long-term hydrologic monitoring and geochemical sampling (**Fig. 1d-g**). Locations PLM1, 2, and 3 on the hillslope were instrumented for depth-resolved measurements to as deep as 8.2 m below ground surface (bgs). Note that the location PLM3 is at the toe-slope, and the mid-slope location PLM2 is elevated by about 2 m relative to the average hillslope profile. At the floodplain location PLM4, samplers and instruments were installed to a maximum depth of only 1.28 m due to the original borehole collapsed prior to instruments installation. Location PLM6, located 4.5 m away from PLM3 at the same elevation, was drilled to recover continuous core samples and to install a groundwater monitoring well; it does not contain depth-distributed instrumentation. The water table depth below the local soil surface at PLM1 and PLM6 was continuously recorded with pressure transducers (AquaTROLL 200). At all of the other PLM locations, water table depths were determined from equilibrium pressure measurements in porewater samplers using the “tensisampler” method and from depth-distributed moisture sensors. At PLM4, depths to the water table were also obtained from the correlation between locally measured groundwater levels and continuously measured East River water levels.

Soil and rock sampling and analyses. Soil thickness of along the hillslope was measured by using hand-auger (0.07 m diameter) in 0.10 m depth increments down to as deep as the auger could be advance. The soil thickness is defined as the depth at which the manual core sampling was no longer possible (meets the rock). Based on 40 hand-cored soil samples, the soil depths are 0.9-1.1 m, 0.7-0.9 m, and 1.0 -1.3 m bgs at stations PLM 1, 2, and 3, respectively. Thus, the soil depths on this hillslope are approximately 1.0 ± 0.3 m bgs. At PLM4, the soil depth is 0.7-0.8 m bgs. These hand-augered soil samples were later used for chemical and mineral analyses. Roots, only found in the shallow soil samples above about 20 cm, were removed before further sample processing. Deeper than approximately 1 m bgs, rock samples were collected in 0.6 to 0.7 m depth increments from boreholes at locations PLM1–4 and PLM6. The soil and rock samples were oven dried at 75°C for three days, then milled to grain sizes less than about 50 μm for the following analyses. Solid phase elemental compositions were determined using X-ray fluorescent (XRF) by the Geochemistry Division of the commercial laboratory ALS Global

(<http://www.alsglobal.com/geochemistry>), with an analytical uncertainty < 0.1% based on 3 replicate measurements. Mineralogical analyses were conducted using quantitative X-ray diffraction (XRD) by the commercial laboratory Xrayminerals (<http://www.xrayminerals.co.uk>), with relative uncertainties < 10%. Total nitrogen contents were determined using elemental analyses (EA) by the Isotope Core Laboratory at Washington State University (<https://www.isotopes.wsu.edu>), with relative uncertainties < 3%. Inorganic carbon (IC) and organic carbon (OC) were determined using a Shimadzu TOC-VCSH carbon analyzer by our own LBNL/EESA Aqueous Geochemistry Lab with relative uncertainty < 1%.

Relative concentrations $\tau_{i,j}$ of weathering profile elements^{32,33} were defined by

$$\tau_{i,j} = \frac{C_{j,w} C_{i,p}}{C_{j,p} C_{i,w}} - 1 \quad (1)$$

where C is concentration, the subscript j represents a mobile constituent (element or mineral of interest), and subscript i represents the immobile reference element titanium (Ti) associated with the parent rock. In the calculations we used as the immobile element i . Subscripts w and p denote weathered and parent rock, respectively. The concentrations of element/mineral j and i in parent rock were determined by averaging their respective parent rock concentrations.

Fluid phase sampling and analyses. The water leachates of soil-rock samples were obtained using an artificial groundwater recipe of 5 mM CaCl₂ and 5 mM NaCl in equilibrium with atmospheric CO₂. The solid:water ratio is 1:10. The soil-rock solid samples were powdered to about 50 µm. After 24 hours slow mixing on a reciprocating shaker, the aqueous phase was separated by centrifugation and filtration (0.45 µm). The NH₄⁺ concentration was analyzed immediately, and then the TDN and NO₃⁻, using analytic methods described later.

Porewater were collected from the depth-distributed lysimeters at about monthly intervals from fall 2016 to winter 2019, and approximately 3 times per month in spring to summer in 2019. The collected porewaters were immediately filtered at the field (0.45 µm polytetrafluoroethylene syringe filters), and divided into subsamples for different types of analyses. The samples were shipped overnight to the laboratory in a cooler containing ice packs, and refrigerated or frozen for later analyses.

Pore-water cation concentrations were measured using an inductively coupled plasma mass spectrometer (Thermo Fisher, MA, USA). Anions including NO₃⁻ and NO₂⁻ were measured using Ion Chromatograph (Dionex ICS-2100, Thermo Scientific, USA), with precisions of ±5% of reported values. Dissolved organic carbon (DOC) and inorganic carbon (DIC) were determined using a TOC-VCPH analyzer (Shimadzu Corporation, Japan). DOC was analyzed as non-purgeable organic carbon (NPOC) by purging acidified samples with carbon-free air to remove DIC prior to measurement. Total dissolved nitrogen (TDN) was analyzed using a Shimadzu Total Nitrogen Module (TNM-1) combined with the TOC-VCSH analyzer (Shimadzu Corporation, Japan), with the precisions ±3% of reported values. All nitrogen species in samples are combusted to nitrogen monoxide and nitrogen dioxide, then reacted with ozone to form an excited state of nitrogen dioxide. Upon returning to ground state, light energy is emitted and TN is measured using a chemiluminescence detector. For DOC/DIC/TDN in porewater samples, the relative standard deviation (RSD) < 3% was estimated from 3-5 replicates. Ammonia (NH₄⁺) was determined using a Lachat's QuikChem® 8500 Series 2 Flow Injection Analysis System (LACHAT Instruments, QuikChem® 8500 series 2, Automated Ion Analyzer, Loveland, Colorado). The RSD < 3% is obtained based on 2 replicate measurements. Pore-gas samples

were collected from the depth-distributed pore-gas samplers in subsurface unsaturated regions. At the field the extracted gas from certain depth was injected and slightly over-pressurized into 50 ml pre-evacuated serum glass vials sealed with 14 mm-thick chlorobutyl septa (Bellco Glass, Inc.). Concentrations of CO₂, N₂O, and CH₄ were analyzed using a Shimadzu Gas Chromatograph (GC-2014), with a precision of ±5% of the reported value.

Porewater fluxes calculations. Downslope flow of pore waters was determined based on calculations of water table elevation-dependent Darcy fluxes in the fractured bedrock, WZ, and soil. Briefly, flow in each of these zones was equated with the product of its hydraulic conductivity K , its saturated thickness, and the hydraulic head gradient. Subsurface water fluxes were calculated using two scenarios in order to constrain predictions. One scenario was based on the field-measured K in each zone, and another used K that are greater than field-measured values, recognizing that local measurements of K commonly yield values that are too low to represent hillslope-scale flow. For the field measurements-based case, K values of the surface soil, subsoil, WZ, and fractured bedrock were assigned values of 9.7×10^{-6} , 7.9×10^{-6} , 1.1×10^{-5} , and $1.6 \times 10^{-7} \text{ m s}^{-1}$, respectively. The saturated thicknesses of each zone were determined with continuous piezometer (pressure transducer) measurements. Piezometric measurements showed that the hydraulic head gradient remained very close to the slope of the soil surface along the transect, and the much higher K of shallower zones relative to the fractured bedrock supported application of the transmissivity feedback approach^{40,46} for describing subsurface flow. Given the large uncertainties associated with K , as well as observations that K measurements obtained in small boreholes in soil are often much lower than that associated with the field scale K measurements⁴⁷, subsurface flow calculations were also performed with K values in the soil and WZ that were 25- and 1.5-times higher than their respective field-measured values. A water mass balance constraint was applied such that the total precipitation (872 mm) minus calculated evapotranspiration (310 mm) for water year (WY) 2017 was balanced by the transmissivity-based total subsurface flow over the same period. That mass balance constraint prevented assigning larger amplifications to the measured WZ K because all subsurface flow would then have to be accommodated within depths shallower than 10 m bgs, contrary to field observations. The water mass balance constraint also led to setting the depth to the operationally defined impermeable boundary at the bottom of the fractured bedrock at 176 and 29.8 m bgs, for flow calculations based on the measured and enhanced K values, respectively.

Rock weathering rates calculations. From our previous study⁴¹, weathering rates were calculated from the export of base cations (BC: Na⁺, K⁺, Ca²⁺, and Mg²⁺). Although pore water specific conductance (SC, $\mu\text{S}/\text{cm}$) was presented as functions of time and depths to represent trends in overall ion concentrations in **Fig. S2**, sums of actual BC equivalent charge concentrations were used in the weathering rate calculations. The linear correlation between SC and BC (the sum of Na⁺, K⁺, Ca²⁺, and Mg²⁺ equivalents) was determined from a representative subset of pore water samples, yielding $\text{BC}(\text{mM}_c) = 0.0105(\text{mM}_c/(\mu\text{S}/\text{cm})) \cdot \text{SC}$ ²⁷. BC weathering rates are commonly normalized per unit area of watershed. Therefore, the product of flow rate times BC concentration was normalized on a daily basis to the area of the transect and its contributing upslope region to obtain the daily BC discharge rate. Two improvements were made over the previous weathering rate calculations. First, the integrated BC weathering rates were obtained by summing over 365-day intervals. It should be noted that the measured BC concentrations in the fractured bedrock zone were scaled by a factor of 0.608 for export

calculations based on the measured K profiles because the bedrock flow is calculated to extend down to 176 m bgs. This adjustment was made because our bedrock pore waters were sampled at only 3.7 to 8.2 m bgs where solute concentrations are relatively high due to the influence of the overlying WZ. The factor 0.608 is the ratio of average BC in a 60 m deep Mancos Shale well to the average in the PLM hillslope bedrock. The 60 m deep well is located 5.0 km upstream within the East River watershed. The second improvement consists of adding more recent measurements and now averaging over nearly three years of pore water data. The resulting BC weathering rate of $55.3 \pm 4.4 \text{ kmol}_c \text{ ha}^{-1} \text{ y}^{-1}$ represents the average of exports based on the measured K profiles and enhanced K profiles, with the uncertainty range spanning these two K scenarios.

Rock-N weathering rates calculations. The BC weathering rates were scaled by the concentration ratio of rock-N to the BC, following similar applications of rock mass balance^{9,39}. Scaling the BC weathering rates by the measured ratio of rock N:BC of 0.0244 yielded rock-N release rates of 1.74 and 1.52 $\text{kmol N ha}^{-1} \text{ y}^{-1}$ for the measured and enhanced K scenarios, respectively. The average and difference between these two values are taken as the best estimate rock-N release rate and its uncertainty, which on a mass basis amounts to $18.9 \pm 1.5 \text{ kg N ha}^{-1} \text{ y}^{-1}$.

Total dissolved nitrogen (TDN) export rate calculations. In the transmissivity feedback approach, the daily advective transport of TDN is calculated as the product of the Darcy flux times the TDN concentration within each zone. For this purpose, TDN concentration data from the three hillslope locations were combined to obtain time trends characteristic of the soil, WZ, and fractured bedrock. Specifically, the average TDN values (averages for days with 3 or more individual sample analyses obtained within a given zone) served as the basis for generating continuous TDN concentration curves for each zone. TDN values for unsampled days were assigned through interpolating between nearest sampled days. For the large data gap between September 29, 2018 and April 22, 2019, the average of all TDN concentration data within a given zone was applied for days in which the water table remained within the zone. Long periods during which the water table resides below the soil-WZ interface do not contribute to downslope flow along the soil zone. Thus, the average of all measured fractured bedrock TDN concentrations was applied throughout this long gap for the bedrock, while the average WZ TDN was applied from September 29, 2018 through January 25, 2019 (after which the water table declined below the WZ).

N₂O emission rate calculations. Rates of N₂O diffusion at the soil surface at three hillslope locations were calculated following a procedure previously used for determining CO₂ fluxes⁴⁴. The N₂O concentrations measured on samples collected from the shallowest gas samplers were used with the atmospheric N₂O concentration (330 ppb) and sampler depth (0.30, 0.28, and 0.20 m, for PLM1, PLM2, and PLM3, respectively), to calculate the concentration gradient. N₂O gradients were determined on a daily basis, interpolating between measured days. For the large data gap from August 23, 2018 to May 10, 2019, the average of all measured gradients was used for each location. The effective diffusion coefficient for N₂O in soil D_e was calculated with the water-induced linear reduction model applied to Marshall's model⁴⁸,

$$D_e = D_o \varepsilon^{2.5} \Phi^I \quad (2)$$

where ε is the air-filled porosity, Φ is the total porosity, and D_o is the diffusion coefficient for N₂O in the bulk air phase. Adjustments were applied to Massman's N₂O D_o formula⁴⁹ is using the

daily average temperature recorded by the shallowest matric potential sensor (Decagon MPS6) and average local atmospheric pressure of 72.2 KPa estimated with the Boltzmann barometric equation for the average hillslope elevation of 2776 m. Total porosities, matric potentials, and volumetric water contents needed for calculating D_e were obtained from core sample measurements at adjacent locations and sensors (Decagon 5TE and MPS6), respectively. Specific values for Φ for the midplane of the shallowest interval at PLM1, PLM2, and PLM3 were assigned 0.58, 0.59, and 0.63, respectively, based on a third-order polynomial fit of data on the depth dependence of shallow soil bulk densities and an assumed solid density of 2.65 g cm⁻³. Volumetric water contents were calculated by combining field matric potential sensor measurements with laboratory pressure plate moisture measurements on shallow soil samples, and with field soil moisture sensors (Decagon 5TE), then subtracted from Φ to obtain ε . Fickian N₂O fluxes were calculated as the product of the D_e and the N₂O concentration gradient on a daily basis.

During periods with snowpack, N₂O concentrations increase above 330 ppb at the soil-snow interface, and the interface N₂O concentration requires estimation. For negligible storage within the snowpack, the diffusive fluxes of N₂O through the surface soil and snowpack are equal

$$D_e \frac{(C_1 - C_b)}{z_1} = D_{snow} \frac{(C_b - C_0)}{z_2} \quad (2)$$

Where C_1 , C_b , and C_0 are the N₂O concentrations in the shallowest gas sampler, at the soil-snow boundary, and in the atmosphere, respectively, D_{snow} is the effective diffusion coefficient of N₂O through snow, and z_1 and z_2 are the depth of the shallowest soil gas sampler and the thickness of the snowpack, respectively. Values of D_{snow} were estimate based on the linear reduction model (eq. 2), with ε identical to Φ_{snow} , using daily snow densities measured at the nearby snow telemetry station (Butte SNOTEL). The snowpack thicknesses z_2 were estimated from a linear regression between measurements obtained along the hillslope transect during 2017 and 2020, and thicknesses reported from the Butte SNOTEL. Values of C_b were calculated for serial, steady-state diffusion through the surface soil and snowpack as

$$C_b = \left(\frac{z_2 D_e}{z_1 D_{snow} + z_2 D_e} \right) C_1 + \left(\frac{z_1 D_{snow}}{z_1 D_{snow} + z_2 D_e} \right) C_0 \quad (4)$$

It should be noted that the calculated diffusive fluxes are likely underestimates because wind is expected to enhance gas fluxes through snow⁵⁰.